

# Fabrication of nano-grained Ti–Nb–Zr biomaterials using spark plasma sintering



M.A. Hussein<sup>a,b</sup>, C. Suryanarayana<sup>c</sup>, N. Al-Aqeeli<sup>a,\*</sup>

<sup>a</sup> Department of Mechanical Engineering, King Fahd University of Petroleum & Minerals, Dhahran 31261, Saudi Arabia

<sup>b</sup> Department of Mechanical Engineering, Kafrelsheikh University, Kafrelsheikh 33516, Egypt

<sup>c</sup> Department of Mechanical and Aerospace Engineering, University of Central Florida, Orlando, FL 32816-2450, USA

## ARTICLE INFO

### Article history:

Received 10 June 2015

Received in revised form 12 August 2015

Accepted 17 August 2015

Available online 20 August 2015

### Keywords:

Biomaterials

Spark plasma sintering

Mechanical alloying

Nanomaterials

Ti–Nb–Zr alloy

## ABSTRACT

Nanostructured near- $\beta$  Ti–20Nb–13Zr at % alloy with non-toxic elements and enhanced mechanical properties has been synthesized by spark plasma sintering (SPS) of nanocrystalline powders obtained by mechanical alloying. The consolidated bulk product was characterized by density measurements and Vickers hardness (HV), and X-ray diffraction (XRD), field emission scanning electron microscopy (FE-SEM) combined with energy-dispersive spectroscopy (EDX), and transmission electron microscopy (TEM) for structural details. The temperature during spark plasma sintering was varied between 800 and 1200 °C, while the heating rate and holding time of 100°K/min and 10 min were maintained constant in all the experiments. The effect of SPS temperature on the densification, microstructure, and HV was discussed. The results show that a nearly full density structure was obtained after SPS at 1200 °C. The microstructure of the obtained alloy is a duplex structure with the  $\alpha$ -Ti (hcp) region having an average size of 70–140 nm, surrounding the  $\beta$ -Ti (bcc) matrix. The obtained alloy was chemically homogenized with a micro hardness value, HV of 660. The developed nanostructured Ti–20Nb–13Zr alloy is suggested for biomedical use as in implant material in dental and orthopedic applications.

© 2015 Elsevier Ltd. All rights reserved.

## 1. Introduction

A number of different metallic materials have been used in a variety of applications in the medical field. Specifically, they are used for internal support and biological tissue replacements such as joint replacement, dental roots, orthopedic fixation and stents [1]. The common metals and alloys that are being utilized for biomedical applications are: stainless steels, Co-based alloys, and Ti-based alloys. However, Ti and Ti-based alloys have dominated over other alloy systems in the medical and dentistry fields due to their improved biocompatibility [2–4]. Many Ti-based alloys were developed with the addition of multiple alloying elements in order to evaluate their individual contributions and arrive at an improved composition that possesses the highest biocompatibility. Different metals like vanadium, nickel, chromium, and aluminum were added via different processing routes and some Ti-based alloys were introduced, e.g., Ti–6Al–4 V [5]. However, it was observed that vanadium and aluminum are probably toxic [2] and can cause mutagenic cytology in addition to triggering allergic reactions [3]. Other constituents like nickel were found to result in lower biocompatibility [5] and chromium has a major concern due to its genotoxicity [5]. Therefore, both the selection of alloy composition and finding the best

processing method to develop Ti-based alloys have been a challenge in the biomedical/biomaterials field.

All the three constituents in the Ti–Nb–Zr alloy meet the criteria for biomaterials in terms of biocompatibility, resistance to corrosion, mechanical considerations, and ionic cytotoxicity [5]. The addition of Nb to Ti allows stabilizes the  $\beta$  phase in these alloys and possess improved mechanical properties, and also results in improved wear resistance, while the addition of Zr helps in obtaining the solid solution required for achieving the hardness [2].

There has been some work reported in the literature on the development of Ti-based alloys using arc melting and casting techniques [2,3,6–12]. However, when there is a broad range of melting temperatures between the alloy constituents, utilization of conventional casting techniques in the synthesis of Ti-based alloys does not seem to be an optimal route due to plausible absence of homogeneity in the final alloy. Therefore, mechanical alloying (MA), a completely solid-state powder processing technique, can be considered as a promising alternate technique to combat limitations faced by casting techniques. MA has also been used successfully in the development of nanostructured materials. This technique is known to be simple, versatile, economically viable and can be scaled up to produce large quantities [13]. Powder metallurgy (PM) processing is also considered to be an effective way in reducing the higher machining costs of Ti alloys. It has the advantage to produce a homogenous alloy compared to other techniques, especially when the alloying element has a higher melting temperature such as Nb [4].

\* Corresponding author.

E-mail addresses: [mahussein@kfupm.edu.sa](mailto:mahussein@kfupm.edu.sa) (M.A. Hussein), [Surya@ucf.edu](mailto:Surya@ucf.edu) (C. Suryanarayana), [naqeeli@kfupm.edu.sa](mailto:naqeeli@kfupm.edu.sa) (N. Al-Aqeeli).

Nevertheless, the production of net-shape parts of MA samples needs to go through the challenge of consolidation as the product of MA is always in the powder form. The situation becomes even more challenging when the produced alloys from MA are having nanostructures since the high temperatures associated with conventional consolidation techniques, such as hot isostatic pressing, can induce undesirable grain growth.

Spark Plasma Sintering (SPS) is considered a non-conventional and new sintering technique and is classified as a rapid consolidation technique [14,15]. SPS has already been used by several researchers to synthesize Ti-based alloys. Xu et al. [16] used MA and SPS to produce a fine-grained Ti–43Al–9V alloy. Ileana and Oana [17] successfully obtained the Ti alloy by SPS starting from hydride ( $\text{TiH}_2$ ) powders. Stir et al. [18] used SPS to produce a fully dense CP Ti, Ti–Al–V, and porous structure in Ti–Al–V–Cr and Ti–Mn–V–Cr–Al alloys. Recently, Wen et al. [19] developed Ti–Nb–Ag alloys using both conventional vacuum sintering and SPS. They noted that the fracture strength of the samples obtained by SPS was three times that obtained by conventional sintering. More recently, Hussein, et al. [20] synthesized ultrafine/nanostructured Nb–Zr alloy with an average grain size between 100 and 300 nm by MA and SPS. The developed alloy exhibited high corrosion resistance in simulated human body fluid (SBF) medium. The Nb content was reported to improve the corrosion resistance of binary Nb–Zr alloy [21], and to increase the wear resistance of the Ti–Nb–Ta–Zr alloy [22].

In this paper, we report, for the first time, the synthesis of a nanostructured Ti–20Nb–13Zr (at.%) alloy by MA and SPS techniques. The Ti–20Nb–13Zr at.% powder alloy were prepared by MA starting from elemental Ti, Nb, and Zr powders as raw materials, and then consolidated using the SPS technique. The effect of SPS processing temperature on the final microstructure, microhardness, and densification behavior of sintered samples was investigated.

## 2. Experimental methods

Elemental powders of titanium, niobium, and zirconium (of – 325 mesh size and 99.8% purity), supplied by Alfa Aesar, were used as starting materials. The powders were mixed in an atomic percentage of 20%Nb and 13%Zr (rest Ti). The mixture was weighed and loaded in a tungsten carbide vial with tungsten carbide balls to give a ball to powder weight ratio of 10:1. The powders were mechanically alloyed (MA) for 10 h under argon atmosphere in a planetary ball mill (Fritsch Pulverisette 5) with a rotational speed of 300 rpm without the addition of any process control agent to avoid contamination of the powder. The MA'd powders were sintered using the spark plasma sintering (SPS) machine (FCT system-model HP D5, Germany). The powders MA'd for 10 h were loaded into 20 mm graphite die and punch. A thin graphite foil was used between the powders and the die to facilitate sample ejection after sintering and to reduce the friction between the die walls and the powders. The SPS experiments were conducted in vacuum at a pressure of 50 MPa. The heating rate and holding time were selected to be 100°K/min and 10 min, respectively. The sintering temperatures were chosen to be 800, 900, 1000, 1100, and 1200 °C. A thermocouple inserted into the die was used to measure the temperature. After SPS, the sample was polished to remove surface contamination from carbon. From the previous work of the authors [20], we found that the samples sintered at holding time of 10 min possess higher microhardness compared to the samples sintered at 15, and 25 min, as the increase in holding time results in higher growth of the grains and ultimately lower hardness values [20]. Also, we found that the decrease in heating rate from 100 to 50°K/min enhance the HV [20]. However, it leads to increase in the grain size (unpublished results). So, we used in this study heating rate and holding time of 100°K/min and 10 min respectively to minimize the grain growth.

The phases present in the MA'd powders and SPS samples were studied via X-ray diffraction (XRD) using the AXSD8 Bruker machine with Cu-K $\alpha$  radiation and at a scanning speed of 1°/min. A field emission scanning electron microscope (FE-SEM), (Tescan Lyra-3) equipped

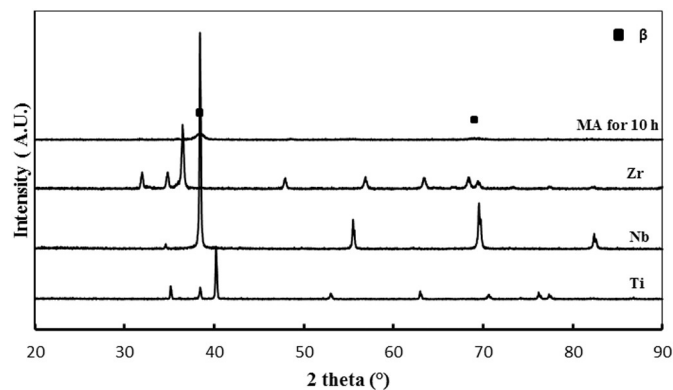


Fig. 1. XRD patterns of the as-received elemental powders and the blended elemental Ti–20Nb–13Zr powder milled for 10 h.

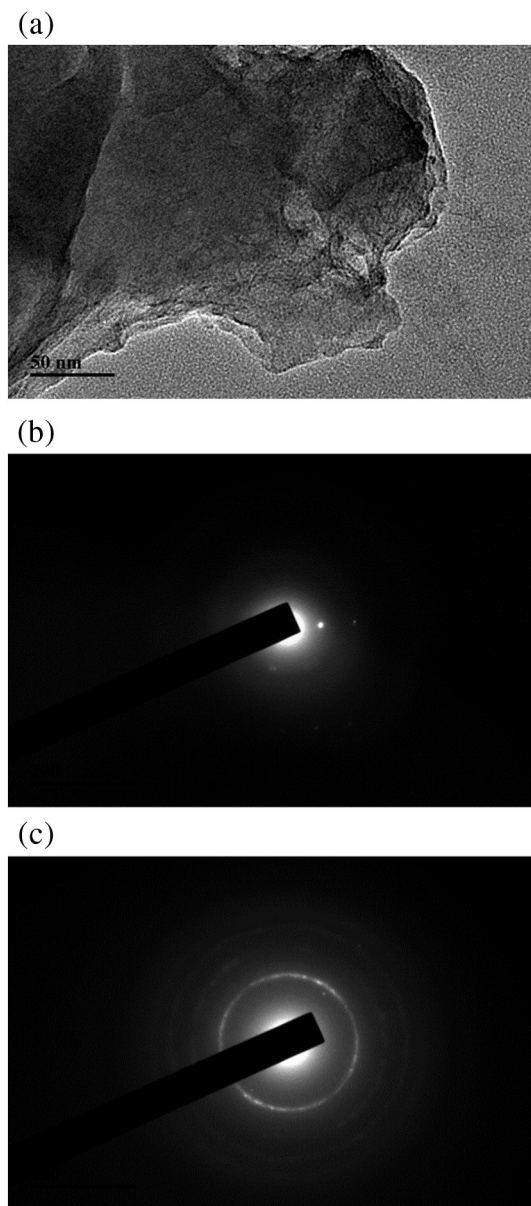


Fig. 2. (a) Bright field TEM image and selected area diffraction patterns from the (b) amorphous and (c) crystalline regions of the Ti–20Nb–13Zr powder milled for 10 h.

with the energy-dispersive X-ray (EDX) analysis was used to characterize the morphology of the powders, microstructures, and chemical compositions for both the MA'd powders and SPS samples. The microstructures were also examined using a transmission electron microscope (TEM: Tecnai G Series operated at 200 keV). The SPS samples were etched with 10%HF solution for 5 s to reveal the microstructural details on FE-SEM. A hardness tester (Buehler, USA) with 500 g load and 10 s dwell time was used to measure the microhardness of the consolidated samples after polishing. The density determination kit (Mettler Toledo) was used to measure the density of the sintered samples based on Archimedes principle. The reported values were the average of ten measurements for HV and three measurements for the density.

### 3. Results and discussion

Fig. 1 shows the XRD patterns of the as-received elemental powders and the Ti–20Nb–13Zr powder blend after MA for 10 h. All the expected

peaks for the as-received powders are present. However, after 10 h of milling, the intensity of the diffraction peaks decreased and the peak width increased due to accumulation of mechanical strain and reduction in the crystallite size [23,24]. The XRD pattern of the powder after milling for 10 h shows a mixture of the  $\beta$ -Ti phase, and a partial amorphous phase as evidenced by the diffraction peaks replaced by a broad diffuse halo at the position of the (110) peak of Nb and another peak at the (211) peak position of Nb. It may be useful to remember here that both  $\beta$ -Ti and Nb have the same crystal structure and almost similar lattice parameters. That is why the  $\beta$ -Ti peaks are coinciding with those of Nb. The dissolution of Nb and Zr into Ti and formation of partial amorphous phase may be due to evolution of crystal defects during MA [23]. Formation of a partially amorphous phase was earlier reported by the authors at the same MA conditions in the binary Nb–Zr system [25,26]. To confirm the results obtained from XRD, a TEM study was conducted. Fig. 2 shows the bright field (BF) image and selected area diffraction patterns (SADP) of the Ti–20Nb–13Zr powder

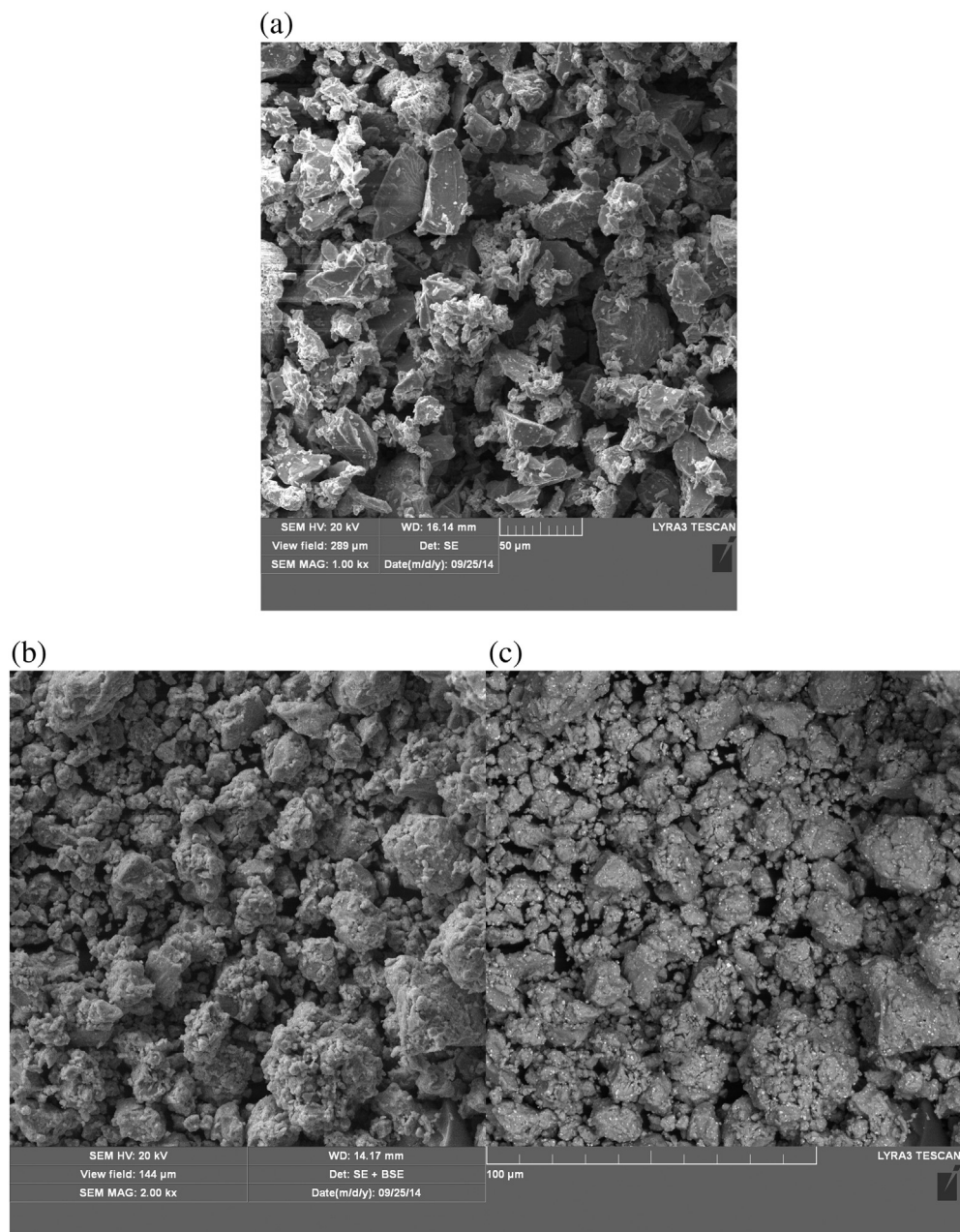


Fig. 3. SEM micrographs of (a) as-received Ti–20Nb–13Zr blended powders, (b) SE image of powder milled for 10 h, and (c) BS image of powder milled for 10 h.



milled for 10 h. Some regions in the powder milled for 10 h clearly show the presence of an amorphous phase. This is confirmed from the high-resolution TEM micrograph that shows the salt-and-pepper like contrast (Fig. 2a) and the presence of a broad diffuse halo in the diffraction pattern (Fig. 2b). The existence of a crystalline phase is also confirmed by the presence of sharp diffraction rings (Fig. 2c). This clearly suggests the co-existence of both amorphous and crystalline phases in the Ti–20Nb–13Zr powders milled for 10 h, confirming the XRD observations.

Fig. 3 presents the SEM micrographs of the Ti–20Nb–13Zr powder blend showing the morphology before and after MA. It can be seen that the raw initial powder blend before MA has different irregular and elongated shapes with an average particle size of 23  $\mu\text{m}$  for Ti and Nb and 31  $\mu\text{m}$  for Zr. The secondary electron (SE) and back scattered (BS) images showing the morphology of the Ti–20Nb–13Zr powder after MA for 10 h are shown in Fig. 3(b) and (c), respectively. By comparison, it is clear that the average particle size in the MA condition is reduced and that the shape of the powder particles is spherical and more uniform compared to the irregular shape that existed in the as-received powders. Some large particles have also appeared due to agglomeration of the smaller particles and excessive cold welding.

Additionally, EDX elemental mapping was done to reveal the distribution of the constituent elements in the MA'd powders. Fig. 4 shows the homogeneous distribution of Ti, Nb, and Zr in the whole area, confirming effective alloying of the powders on milling for 10 h. MA was stopped at this time as the target of homogeneous distribution

of the alloying elements has been achieved and also because further milling could lead to contamination from balls and vials.

Fig. 5 shows the FE-SEM images of the Ti–20Nb–13Zr MA'd powder subjected to SPS at different temperatures. It is clear from the microstructure of the sample sintered at 800 °C and 900 °C, Fig. 5 (a and b), that densification is incomplete, as evidenced by the presence of porosity in the samples. The brighter particles in the back-scattered images of the samples sintered at 800 °C to 1000 °C represent Nb [4]. These Nb particles dissolve in both the  $\beta$  and  $\alpha$  regions with increasing sintering temperatures. It appears that the Nb particles have completely dissolved in the samples sintered at temperatures higher than 1000 °C and this is in conformity with the results reported earlier [4]. The dissolution of Nb continues with increasing sintering temperature, associated with increasing volume fractions of both the  $\beta$ -Ti and  $\alpha$ -Ti (hcp) phases [4]. At 1000 °C, Nb still continued undissolved and the equiaxed microstructure of  $\alpha$  uniformly distributed in  $\beta$ -matrix can be clearly seen. The microstructural features of the samples sintered in the range of 1100–1200 °C shows the  $\beta$ -Ti (bcc) matrix surrounded by the  $\alpha$ -Ti (hcp) region. Simultaneous with the complete dissolution of Nb, the alloy is chemically homogenized at SEM resolution level. It can be inferred from the BS-FE-SEM that the dark phase was  $\alpha$ , and the bright phase was  $\beta$ . The microstructural features obtained by SPS of our samples are different from those obtained by conventional sintering of the blended elemental Ti–13Nb–13Zr powder sintered by conventional methods at temperatures  $\geq 1400$  °C [4]. Ti–13Nb–13Zr sintered by

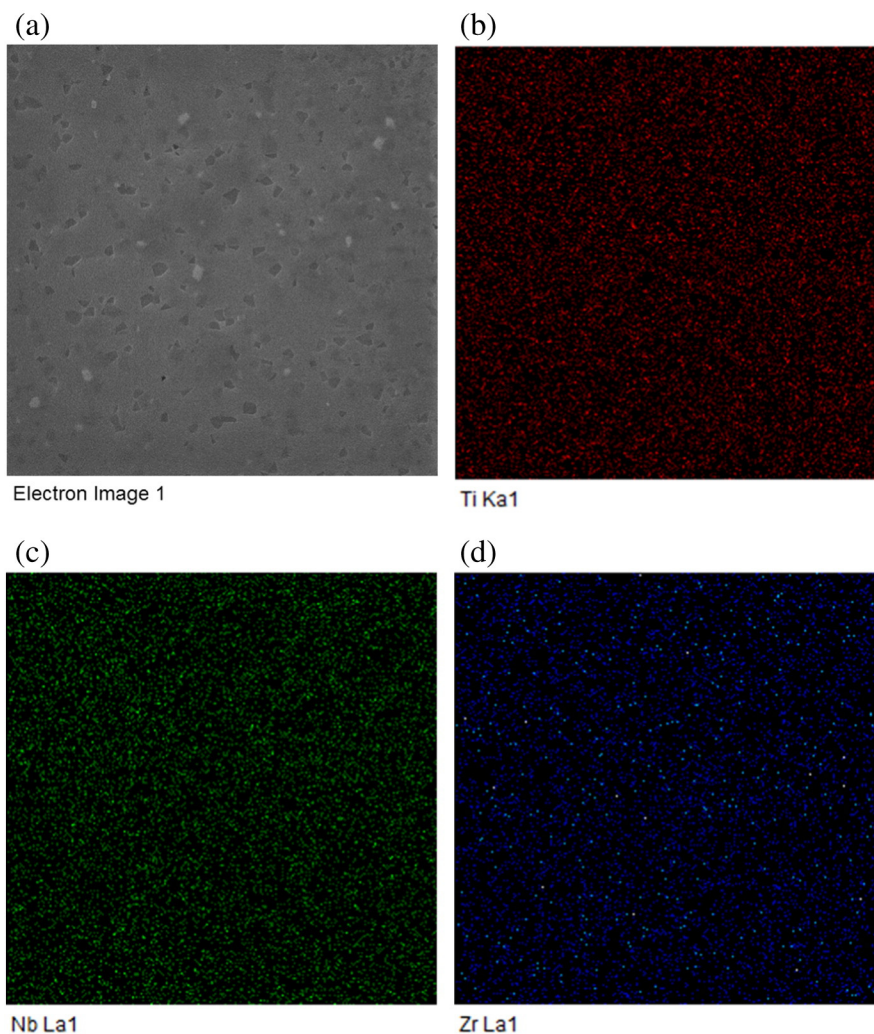


Fig. 4. EDX mapping of the element distribution in the Ti–20Nb–13Zr powder milled for 10 h: (a) scanned area, (b) Ti, (c) Nb, and (d) Zr.

conventional methods showed fine plate-like  $\alpha + \beta$  structure with  $\alpha$  on the grain boundaries [4]. However, in our alloy sintered by SPS, we observed an equiaxed microstructure of  $\alpha$  uniformly distributed in the  $\beta$ -matrix. The equiaxed structure in Ti-based alloys has been reported to possess a better combination of low elastic modulus and higher strength compared to the lamellar or acicular structure [27].

The EDX results from 6 different locations in the Ti–20Nb–13Zr sample sintered at 1200 °C reveal that the average composition of the  $\beta$  phase was Ti–25.26Nb–13.37Zr (at.%), whereas the  $\alpha$  phase contained Ti–18.53Nb–13.84Zr (at.%). The EDX results clearly confirm that the higher Nb content in the  $\beta$ -phase (25.26 at.%) preferentially stabilizes the  $\beta$  phase. Zr is reported to stabilize both  $\alpha$  and  $\beta$  phases in titanium alloys, and accordingly, the Zr content was almost the same (13.4–13.8 at.%) in both the  $\alpha$  and  $\beta$ -phases.

Fig. 6 shows the XRD patterns of the Ti–20Nb–13Zr alloy subjected to SPS at different sintering temperatures. The samples sintered at 800 °C, 900 °C, and 1000 °C revealed peaks from  $\beta$ -Ti,  $\alpha$ , and  $\alpha'$  orthorhombic martensitic phase. The analysis of XRD pattern is challenging as the peaks of Nb and  $\beta$  phase are nearly the same. However, an accurate analysis of the XRD patterns together with the SEM/EDX information confirms that the obtained peaks are for the  $\beta$  phase. The peak intensity of the  $\beta$  phase is higher than that of  $\alpha$  phase indicating that the percentage of  $\beta$  phase is higher than that of the  $\alpha$  phase. The intensity of the  $\alpha'$  (martensitic metastable phase) peak is very low suggesting that it is present only in minor amounts. By increasing the SPS temperature, the amount of  $\alpha'$  decreased and larger amounts of the equilibrium phases ( $\beta$  and  $\alpha$ ) are formed. These results matched with the results obtained from FE-SEM. The results from both BS-FE SEM and XRD

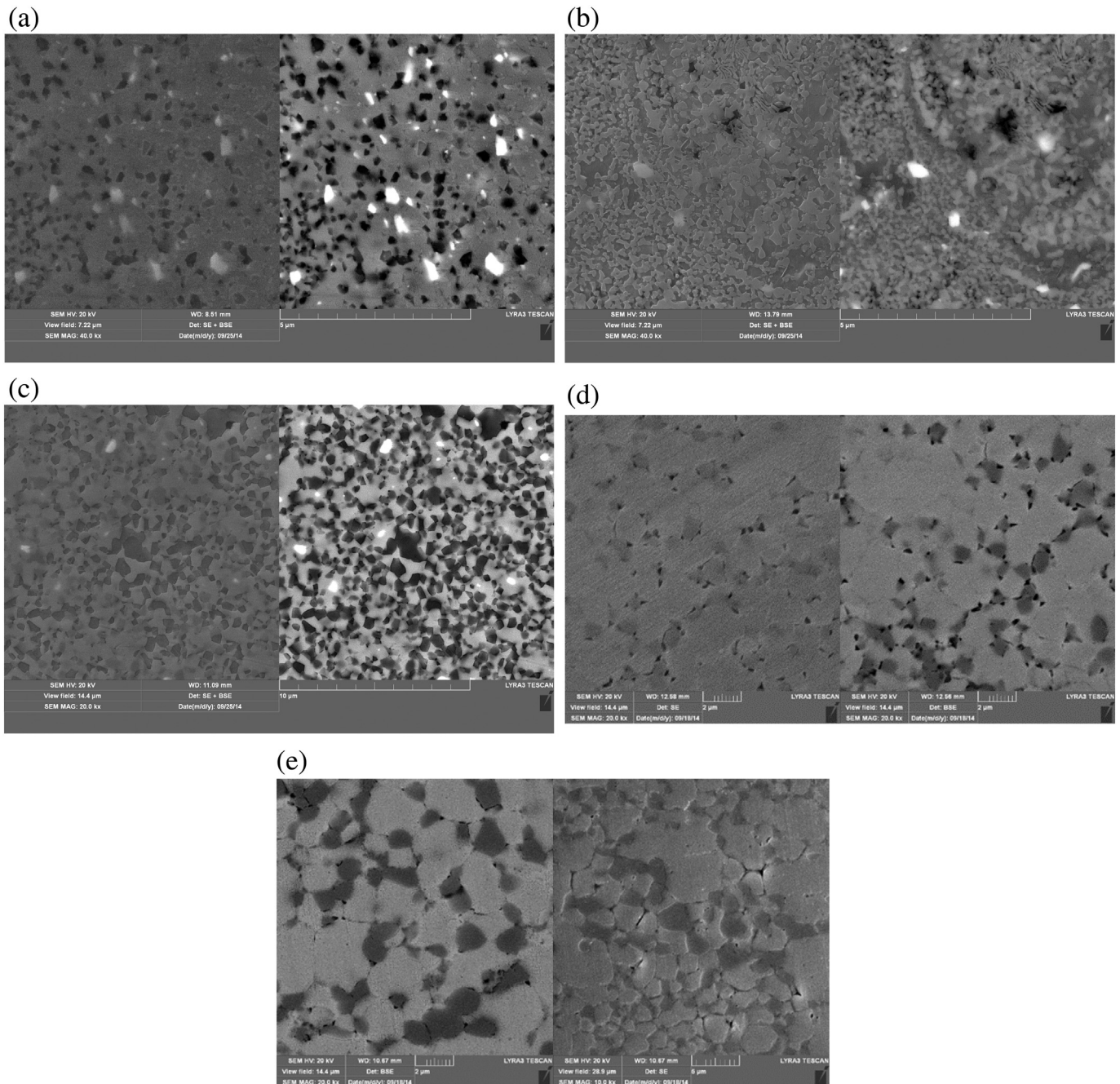
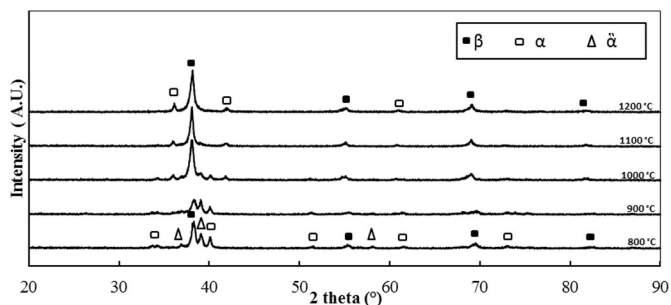


Fig. 5. FE-SEM images of the Ti–20Nb–13Zr alloy after SPS at: (a) 800 °C, (b) 900 °C, (c) 1000 °C, (d) 1100 °C, and (e) 1200 °C. The figure on the left hand side shows the back scattered image while the one on the right hand side shows the secondary electron image.





**Fig. 6.** XRD patterns of the Ti-20Nb-13Zr alloy subjected to SPS at different sintering temperatures. Note that the amount of the  $\beta$ -phase increased with increasing SPS temperature.

suggested that dissolution of Nb continued till 1000 °C, as indicated by the existence of Nb peaks in addition to those of  $\beta$ ,  $\alpha$ , and  $\alpha'$  phases in the samples sintered at 800 °C, 900 °C, and 1000 °C. The increasing intensity of the  $\beta$ -phase peaks with increasing sintering temperature clearly confirmed that the amount of the  $\beta$  phase increased due to dissolution of Nb. Above a sintering temperature of 1000 °C, all the Nb has probably completely dissolved as inferred from the microstructural analysis.

To study the effect of SPS temperature on the densification behavior and Vickers hardness of Ti-20Nb-13Zr alloy, the samples were sintered at heating rate of 100°K/min and 10 min holding time while the sintering temperature was varied. It is clear from Fig. 7(a) that the relative density increased with increasing sintering temperature due to a decrease in the porosity that existed in the specimen. The rate of pore

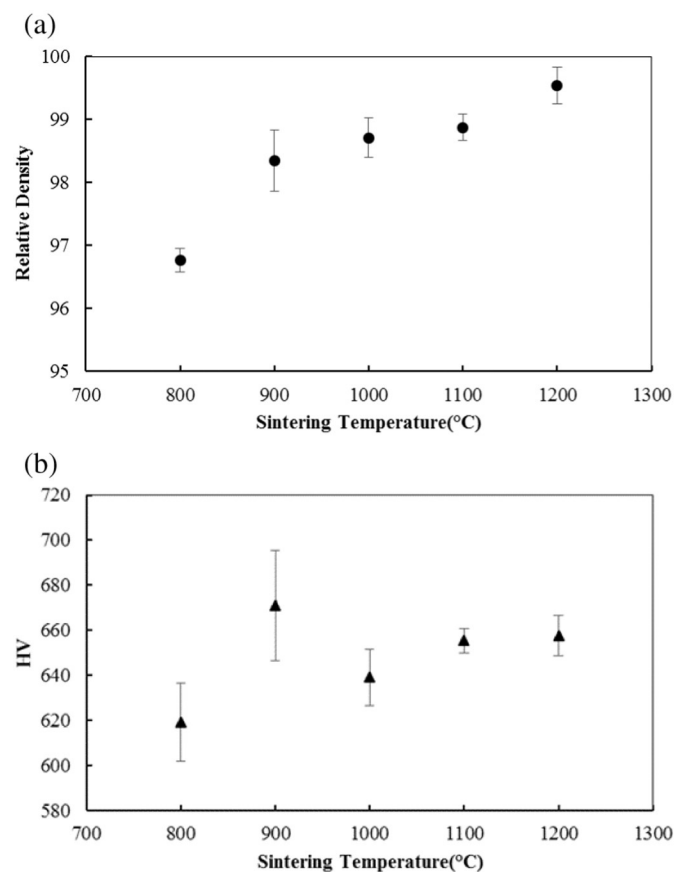


**Fig. 7.** (a) densification, and (b) Vickers hardness of Ti-20Nb-13Zr alloy after SPS at different temperatures.

elimination increased by increasing the SPS temperature which leads to an increase in the relative density of the sample. The samples show a relative density of 96.7% when sintered at 800 °C, which increased slowly with increasing sintering temperature till 99.5% at 1200 °C. The same trend of results was also reported [28,29]. The Vickers micro-hardness of the samples also increased with increasing sintering temperature (Fig. 7(b)); this may be due to a decrease in the number of pores in the resultant sample during heating and the improved contact between the powder particles, even though the trend was slightly different from that of densification [30,31]. The HV increased from 619 at 800 °C to 670 at 900 °C. As can be seen from Fig. 7(b), the hardness of the sample sintered at 1000 °C showed a decrease and then the values started to increase slowly again to 658 at 1200 °C. This latter increase in hardness from 1000 °C to 1200 °C could be attributed to the increased homogeneity in the microstructure. The sample sintered at 900 °C exhibited the highest hardness, even though there is substantial variation in the value with a standard error of 24.4 among all the samples. (This deviation may be related to the different features of the microstructure obtained at 900 °C).

Taddei et al. [32] synthesized the Ti-35Nb-7Zr-5Ta alloy by mixing the metallic powders and cold isostatic pressing and subsequently densifying by conventional sintering. Full densification was achieved at a high sintering temperature of 1700 °C [32]. Also, in the Ti-13Nb-13Zr alloy developed by conventional sintering, the relative density varied between 93 and 97% after sintering at 1400 °C [4]. Compared to these results, it is clear that we were able to obtain by SPS, near fully density in the Ti-20Nb-13Zr alloy, at a much lower temperature. The reason for obtaining a high density in SPS at a relatively lower temperature was due to the ionization of the particles by local sparking during SPS, which causes melting of the titanium oxide films and formation of neck junctions between powder particles at lower temperatures [33]. Additionally, the plasma generated during the SPS process enhances the properties of the sintered powders due to acceleration of interdiffusion between atoms [34].

The hardness and the types of phases present in the nanograined Ti-20Nb-13Zr alloy investigated in this study as well as those other alloys developed for biomedical applications are summarized in Table 1. The listed compositions are in weight percentage unless mentioned otherwise. The hardness values for the samples sintered by SPS are higher than those obtained by conventional sintering methods. These results are in agreements with [35,36]. According to [35] among three consolidation techniques used (SPS, Microwave Sintering ( $\mu$ WS), and Hot Isostatic Press Sintering (HIS), SPS consolidated samples showed the highest HV values. The same conclusion was also drawn by [36], where the HV of SPS of Al6061 and Al2124 alloys samples was also higher than samples sintered by  $\mu$ WS technique.

The increase in hardness of the nanocrystalline materials may be related to the effect of higher dislocation density of smaller grain size [37,38]. According to [39] a high dislocation density was observed in the nanograins sintered by SPS at 950 °C.

**Table 1**  
Comparison of HV and phases in titanium alloys studied.

Alloy composition	Consolidation technique	Phases	HV	Reference
Ti-13Nb-13Zr	Conventional sintering	$\alpha'$	290	[3]
Ti-13Nb		$\alpha'$	340	
Ti-6Al-4 V	Conventional sintering		500	[4]
Ti-13Nb-13Zr		$\alpha + \beta$	300	
Ti-43Al-9V (molar ratio)	SPS	$\gamma$ -TiAl + $\alpha$ 2 Ti <sub>3</sub> Al + B2	592	[16]
Ti-35Nb-7Zr-5Ta	SPS	$\alpha + \beta$	531–668	[45]
Nanocrystalline Ti-20Nb-13Zr (at.%) alloy developed in this study	SPS	$\alpha + \beta$	660	

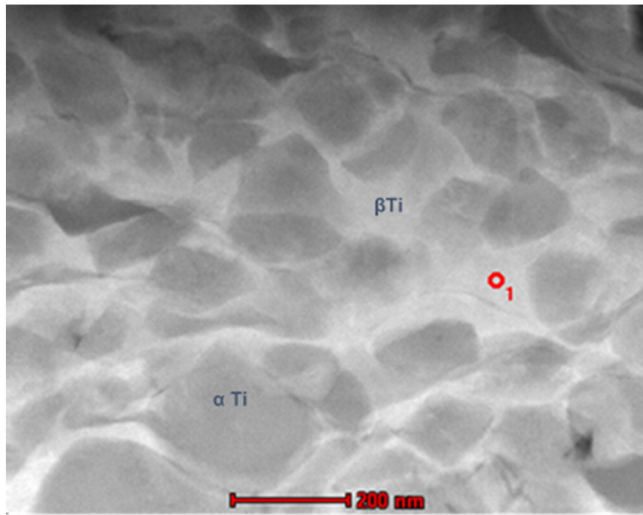


**Fig. 8.** TEM bright field image of the SPS sample sintered at 1200 °C showing equiaxed microstructure of  $\alpha$  uniformly distributed in  $\beta$ -matrix.

According to Hall–Petch relationship, the yield strength is dependent on the grain size and for Vickers indentation, the yield strength ( $\sigma_y$ ) is related to hardness (HV) as  $HV/\sigma_y = 3$ . Therefore, any increase in grain size of SPS samples can result in decrease in hardness [36]. The limits of Hall–Petch relationship was reported to be about at about 20 nm mean grain size [40]. In the current study, the average size of 70–140 nm was obtained, so the Hall–Petch relationship is valid, therefore, the HV increase by decreasing grain size. According to [39] the micron-sized grains obtained by SPS did not exhibit a high dislocation density due to the recrystallization process during SPS, however, a high dislocation density was observed in the nanograins sintered at 950 °C.

In addition, as shown in Table 1, SPS promotes the formation of  $\beta$  phase compared to  $\alpha'$  (hexagonal martensite structure) phase obtained by conventional sintering of Ti–13Nb–13Zr, Ti–13Nb, and Ti–6Al–4V alloys [3]. The Ti–20Nb–13Zr alloy is harder than the Ti–13Nb–13Zr alloy as well as Ti–6Al–4V, due to the increased Nb content, which was reported to enhance the wear resistance of Ti-based alloys [22,41].

One of the criteria that should be stratified in the biomaterial is to have a high wear resistance and exhibit a low friction coefficient when sliding against body tissues to avoid loosen of the implant [42]. The wear resistance is related to the hardness of the materials [41]. The results presented in Table 1 shows that the hardness of the alloy obtained by SPS is higher than obtained by conventional sintering techniques. It was reported in literature that the hardness of the developed alloy depend on the fabrication techniques. For examples, HV of

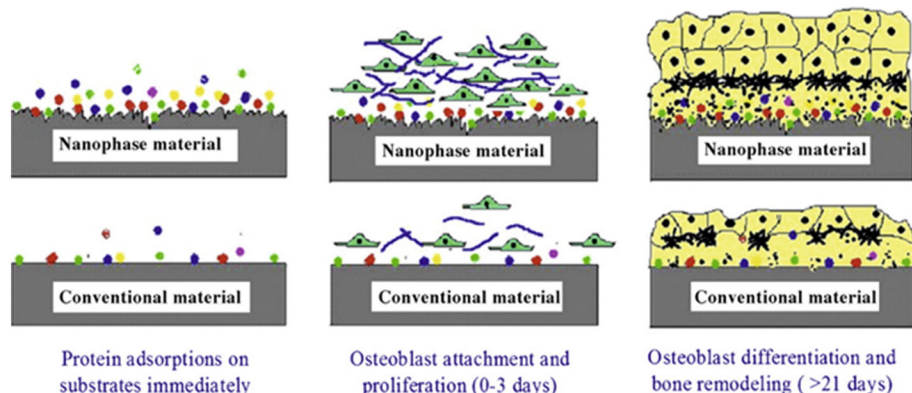
(Co–Cr–Mo) orthopedic alloy sintered by SPS are (683–797) [43]. However, HV of Co–Cr samples fabricated with a direct metal laser sintering (DMLS) technique was reported to be (277–482) [44]. In addition to Forged CoCr alloys exhibit higher wear resistance (related to higher hardness) than cast Co–Cr alloys [41]. For Ti based alloys, the adding Nb to Ti alloys enhances the wear resistance of these alloys because of the increase in the hardness of the alloy [41].

Fig. 8 shows the TEM bright field image of the SPS sample sintered at 1200 °C. The structure is  $\beta$ -Ti (BCC) matrix (bright) which is surrounded by the (hcp) phase (gray). The average grain size of the dispersed  $\alpha$  phase varied between 70 and 140 nm.

The chemical compositions obtained from EDX attached to TEM of the sample sintered at 1200 °C confirmed the coexistence of  $\beta$  phase (white areas) with composition of Ti–(28 ± 1)Nb–(15.6–16.1)Zr (at.%), and  $\alpha$  phase phases (gray areas) with composition of Ti–16.3Nb–(15 ± 1)Zr (at.%) in the obtained microstructure. It is clear from the EDS results that  $\beta$  phase is Nb rich phase as the Nb is preferential stabilization of that phase. However, Zr is stabilizer for both  $\alpha$  and  $\beta$  phases. Which confirm the results obtained by XRD and FE-SEM. These results are in agreement with a trend of results reported in [4].

It has been reported that nanophase materials possess unique surfaces and exceptional mechanical properties similar to those of the human bones; hence they are considered to be the future generation orthopedic biomaterials [46]. Nanocrystalline alloys possess higher surface energy and larger surface area than coarse-grained materials which will lead to enhanced interaction with cells resulting in enhanced proliferation and cell attachment on the nanocrystalline alloy [47]. It was also reported that the surface of metallic materials which possess low micron to nanophase topography enhanced the adhesion of osteoblast (the cells that create the matrix of bone) [48]. Moreover, the nanostructured alloys have better compatibility compared to their coarse-grained counterparts [49]. The bioactive surface of the developed nanostructure alloy promotes greater amount of protein adsorption to stimulate new bone formation than conventional structure as shown in Fig. 9 [50]. In the nanograined materials the number of atoms on the surface is very high and hence possesses large surface energy. Moreover, due to the dimensional similarity to bone/cartilage tissue, nanomaterials also exhibit unique surface properties (such as surface topography, surface chemistry, surface wettability and surface energy) [50]. These advantages of nanocrystalline alloys suggest that the developed nanostructured Ti–20Nb–13Zr alloy is highly suited for biomedical applications as an implant material in dental and orthopedic applications.

A study of the biocompatibility and corrosion resistance in the simulated body fluid of the developed alloy is very interesting and important for the biomaterials requirements. These investigations are currently in progress and the results will be presented and published independently.



**Fig. 9.** The biomimetic advantages of nanomaterials [50].

#### 4. Conclusions

Nanostructured Ti–20Nb–13Zr near- $\beta$  alloy with enhanced mechanical properties was fabricated by mechanical alloying and subsequent spark plasma sintering technique. The main conclusions drawn from the results obtained are as follows:

1. A new nanostructured Ti–20Nb–13Zr near- $\beta$  alloy was developed for biomedical applications. The new alloy contains non-toxic: Ti, Nb and Zr to replace the existing Ti–Al–V which contains toxic elements.
2. The microstructure of the obtained alloy contains a two phase region,  $\beta$ -Ti (bcc) and  $\alpha$ -Ti (hcp). The equiaxed  $\beta$ -Ti (bcc) matrix is surrounded by  $\alpha$ -Ti (hcp) regions, exhibiting an equiaxed structure and chemical homogeneity.
3. The developed nanostructured alloy exhibits a maximum micro-hardness HV of 660, a value higher than reported in the literature.
4. The developed nanostructured Ti–20Nb–13Zr alloy is suggested for biomedical applications as in implant material in dental and orthopedic applications.
5. Solid state synthesis and SPS method is beneficial in prevention of grain growth and synthesis of nanostructured alloys for biomedical applications.

#### Acknowledgments

The authors gratefully acknowledge the financial support from King Fahd University of Petroleum & Minerals (KFUPM) through Project no # IN131020.

#### References

- [1] J. Park, R.S. Lakes, *Biomaterials an introduction*, 3rd ed. Springer, Berlin/Heidelberg, Germany, 2007.
- [2] Ana Lu'cia Roselino Ribeiro, Rubens Caram Junior, Flávia Farias Cardoso, Romeu Belon Fernandes Filho, Luis Geraldo Vaz, Mechanical, physical, and chemical characterization of Ti–35Nb–5Zr and Ti–35Nb–10Zr casting alloys, *J Mater Sci: Mater Med.* 20(2009) 1629–1636.
- [3] K. Niespodziana, K. Jurczk, M. Jurczk, The synthesis of titanium alloys for biomedical applications, *Rev. Adv. Mater. Sci.* 18 (2008) 236–240.
- [4] V.A.R. Henriques, E.T. Galvani, S.L.G. Petroni, M.S.M. Paula, T.G. Lemos, Production of Ti–13Nb–13Zr alloy for surgical implants by powder metallurgy, *J. Mater. Sci.* 45 (2010) 5844–5850.
- [5] A. Biesiekierski, J. Wang, M. Abdel-Hady Gepreel, C. Wen, A new look at biomedical Ti-based shape memory alloys, *Acta Biomater.* 8 (2012) 1661–1669.
- [6] L.W. Ma, H.S. Cheng, C.Y. Chung, B. Yuan, Effect of heat treatment time on microstructure and mechanical properties of Ti–19Nb–9Zr (at.%) shape memory alloy, *Mater. Sci. Eng. A* 561 (2013) 427–433.
- [7] V. Brailovski, S. Prokoshkin, M. Gauthier, K. Inaekyan, S. Dubinskiy, M. Petrzhik, M. Filonov, Bulk and porous metastable beta Ti–Nb–Zr(Ta) alloys for biomedical applications, *Mater. Sci. Eng. C* 31 (2011) 643–657.
- [8] W. Sungtong, A. Khantachawana, Effect of Zr addition on mechanical properties of Ti–Nb–Zr alloys for biomedical applications, *Adv. Mater. Res.* 463–464 (2012) 841–844.
- [9] L. Wang, G. Yang, H. Yang, J. Cao, W. Lü, D. Zhang, Characterization of microstructure and mechanical properties of TiNbZr alloy during heat treatment, *Rare Metal Mater. Eng.* 38 (2009) 1136–1140.
- [10] L.M. Elias, S.G. Schneider, S. Schneider, H.M. Silva, F. Malvisi, Microstructural and mechanical characterization of biomedical Ti–Nb–Zr(–Ta) alloys, *Mater. Sci. Eng. A* 432 (2006) 108–112.
- [11] P. Majumdar, S.B. Singh, M. Chakraborty, The role of heat treatment on microstructure and mechanical properties of Ti–13Zr–13Nb alloy for biomedical load bearing applications, *J. Mech. Behav. Biomed. Mater.* 4 (2011) 1132–1144.
- [12] A.E. Aguilar Maya, D.R. Grana, A. Hazarabedian, G.A. Kokubu, M.I. Luppó, G. Vigna, Zr–Ti–Nb porous alloys for biomedical application, *Mater. Sci. Eng. C* 32 (2012) 321–329.
- [13] C. Suryanarayana, N. Al-Aqeeli, Mechanically alloyed nanocomposites, *Prog. Mater. Sci.* 58 (2013) 383–502.
- [14] M. Oghbaei, O. Mirzaei, Microwave versus conventional sintering: a review of fundamentals, advantages and applications, *J. Alloys Compd.* 494 (2010) 175–189.
- [15] G. Xie, F. Qin, S. Zhu, A. Inoue, Ni-free Ti-based bulk metallic glass with potential for biomedical applications produced by spark plasma sintering, *Intermetallics* 29 (2012) 99–103.
- [16] L.-J. Xu, S.-L. Xiao, Y.-Y. Chen, J. Wang, Microstructure and mechanical properties of Ti–43Al–9V alloy fabricated by spark plasma sintering, *Trans. Nonferrous Metals Soc. China* 22 (2012) 768–772.
- [17] C. Ileana, P. Oana, Bulk titanium for structural and biomedical applications obtaining by spark plasma sintering (SPS) from titanium hydride powder, *J. Therm. Anal. Calorim.* 113 (2013) 849–857.
- [18] M. Stir, B. Nebe, E. Burkel, R. Nicula, F. Lu, Spark plasma sintering synthesis of porous nanocrystalline titanium alloys for biomedical applications, *Biomol. Eng.* 24 (2007) 564–567.
- [19] M. Wen, C. Wen, P. Hodgson, Y. Li, Fabrication of Ti–NbAg alloy via powder metallurgy for biomedical applications, *Mater. Des.* 56 (2014) 629–634.
- [20] M.A. Hussein, C. Suryanarayana, A. Madhan Kumar, N. Al-Aqeeli, Effect of sintering parameters on microstructure, mechanical properties and electrochemical behavior of Nb–Zr alloy for biomedical applications, *Mater. Des.* 83 (2015) 344–351.
- [21] F.Y. Zhou, B.L. Wang, K.J. Qiu, W.J. Lin, L. Li, Y.B. Wang, F.L. Nie, Y.F. Zheng, Microstructure, corrosion behavior and cytotoxicity of Zr–Nb alloys for biomedical application, *Mater. Sci. Eng. C* 32 (2012) 851–857.
- [22] S.J. Li, R. Yang, S. Li, Y.L. Hao, Y.Y. Cui, M. Niinomi, Z.X. Guo, Wear characteristics of Ti–Nb–Ta–Zr and Ti–6Al–4V alloys for biomedical applications, *Wear* 257 (2004) 869–876.
- [23] A. Nouri, X. Chen, Y. Li, Y. Yamada, P.D. Hodgson, C.E. Wen, Synthesis of Ti–Sn–Nb alloy by powder metallurgy, *Mater. Sci. Eng. A* 485 (2008) 562–570.
- [24] C. Suryanarayana, Mechanical alloying and milling, *Prog. Mater. Sci.* 46 (2001) 1–184.
- [25] N. Al-Aqeeli, C. Suryanarayana, M.A. Hussein, Formation of an amorphous phase and its crystallization in the immiscible Nb–Zr system by mechanical alloying, *J. Appl. Phys.* 114 (2013) 153512–153514.
- [26] N. Al-Aqeeli, M.A. Hussein, C. Suryanarayana, Phase evolution during high energy ball milling of immiscible Nb–Zr alloys, *Adv. Powder Technol.* 26 (2015) 385–391.
- [27] M. Niinomi, T. Akahori, Improvement of the fatigue life of titanium alloys for biomedical devices through microstructural control, *Expert Rev. Med. Devices* 7 (2010) 481–488.
- [28] G.M. Le, A. Godfrey, N. Hansen, Structure and strength of aluminum with sub-micrometer/micrometer grain size prepared by spark plasma sintering, *Mater. Des.* 49 (2013) 360–367.
- [29] Z.-F. Liu, Z.-H. Zhang, J.-F. Lu, A.V. Korznikov, E. Korznikova, F.-C. Wang, Effect of sintering temperature on microstructures and mechanical properties of spark plasma sintered nanocrystalline aluminum, *Mater. Des.* 64 (2014) 625–630.
- [30] R.M. German, *Powder metallurgy science*, Metal Powder Industries Federation, Princeton, 1994.
- [31] R.M. German, *Sintering theory and practice*, John Wiley, New York, 1996.
- [32] E.B. Taddei, V.A.R. Henriques, C.R.M. Silva, C.A.A. Cairo, Production of new titanium alloy for orthopedic implants, *Mater. Sci. Eng. C* 24 (2004) 683–687.
- [33] F. Zhang, A. Weidmann, B.J. Nebe, E. Burkel, Preparation of TiMn alloy by mechanical alloying and spark plasma sintering for biomedical applications, *J. Phys. Conf. Ser.* 114 (2009) 1–5 (012007).
- [34] M. Omori, Sintering, consolidation, reaction and crystal growth by the spark plasma system (SPS), *Mater. Sci. Eng.* 287 (2000) 183–188.
- [35] N. Al-Aqeeli, Processing of CNTs reinforced Al-based nanocomposites using different consolidation techniques, *J. Nanomater.* (2013) 1–10.
- [36] N. Saheb, Spark plasma and microwave sintering of Al6061 and Al2124 alloys, *Int. J. Miner. Metall. Mater.* 2 (2013) 152–159.
- [37] A.P. Zhilyaev, T.G. Langdon, Using high-pressure torsion for metal processing: fundamentals and applications, *Prog. Mater. Sci.* 53 (2008) 893–979.
- [38] C. Suryanarayana, Nanocrystalline materials, *Int. Mater. Rev.* 40 (1995) 41–64.
- [39] Somayeh Pasebani, Indrajit Charit, Darryl P. Butt, James I. Cole, Yaqiao Wu, Jatuporn Burns, Sintering behavior of Lanthana-bearing nanostructured ferritic steel consolidated via spark plasma sintering, *Adv. Eng. Mater.* (2015) 1–9.
- [40] S. Yip, Nanocrystals: the strongest size, *Nature* 391 (1998) 532–533.
- [41] M.A. Hussein, A.S. Mohammed, N. Al-Aqeeli, Wear characteristics of metallic biomaterials: a review, *Materials* 8 (2015) 2749–2768.
- [42] J.J. Ramsden, The design and manufacture of biomedical surfaces, *CIRP Ann. Manuf. Technol.* 56 (2007) 687–711.
- [43] Bhairav Patel, Fawad Inam, Mike Reece, Mohan Edirisinghe, William Bonfield, Jie Huang, Arash Angadji, A novel route for processing cobalt–chromium–molybdenum orthopaedic alloys, *J. R. Soc. Interface* 7 (2010) 1641–1645.
- [44] Simel Ayyıldız, Elif Hilal Soyulu, Semra İde, Selim Kılıç, Cumhur Sipahi, Bulent Pişkin, Hasan Suat Gökçe, Annealing of Co–Cr dental alloy: effects on nanostructure and Rockwell hardness, *J. Adv. Prosthodont.* 5 (2013) 471–478.
- [45] L.M. Zou, C. Yang, Y. Long, Z.Y. Xiao, Y.Y. Li, Fabrication of biomedical Ti–35Nb–7Zr–5Ta alloys by mechanical alloying and spark plasma sintering, *Powder Metall.* 55 (2012) 65–71.
- [46] M. Geetha, A.K. Singh, R. Asokamani, A.K. Gogia, Ti based biomaterials, the ultimate choice for orthopaedic implants – a review, *Prog. Mater. Sci.* 54 (2009) 397–425.
- [47] D. Khang, J. Lu, C. Yao, K.M. Haberstroh, T.J. Webster, The role of nanometer and sub-micron surface features on vascular and bone cell adhesion on titanium, *Biomaterials* 29 (2008) 970–983.
- [48] B.C. Ward, T.J. Webster, Increased functions of osteoblasts on nanophase metals, *Mater. Sci. Eng. C* 27 (2007) 575–578.
- [49] T.J. Webster, J.U. Ejirofor, Increased osteoblast adhesion on nanophase metals: Ti, Ti6Al4V, and CoCrMo, *Biomaterials* 25 (2004) 4731–4739.
- [50] L. Zhang, T.J. Webster, Nanotechnology and nanomaterials: promises for improved tissue regeneration, *Nano Today* 4 (2009) 66–80.